

# Stripe quadrupole order in the nematic phase of $\text{FeSe}_{1-x}\text{S}_x$

W.-L. Zhang,<sup>1,\*</sup> S.-F. Wu,<sup>1,†</sup> S. Kasahara,<sup>2</sup> T. Shibauchi,<sup>3</sup> Y. Matsuda,<sup>2</sup> and G. Blumberg<sup>1,4,‡</sup>

<sup>1</sup>*Department of Physics & Astronomy, Rutgers University, Piscataway, New Jersey 08854, USA*

<sup>2</sup>*Department of Physics, Kyoto University, Kyoto, 606-8502, Japan*

<sup>3</sup>*Department of Advanced Materials Science, University of Tokyo, Kashiwa, Chiba 277-8561, Japan*

<sup>4</sup>*National Institute of Chemical Physics and Biophysics, Akadeemia tee 23, 12618 Tallinn, Estonia*

(Dated: October 26, 2017)

We use polarization-resolved electronic Raman spectroscopy to study charge dynamics in non-magnetic  $\text{FeSe}_{1-x}\text{S}_x$  superconductor. We observe two features of the  $XY$  quadrupole symmetry: a low-energy quasi-elastic peak (QEP) and an electronic continuum extending to high energy. The QEP exhibits critical enhancement upon cooling towards the structural transition at  $T_S(x)$ . Below  $T_S(x)$ , the QEP diminishes gradually, and a gap with temperature evolution reminiscent to a mean-field order parameter opens up in the continuum. The intensity of the QEP develops with increasing  $x$ , while the gap magnitude decreases. We interpret development of the gap in the quadrupole scattering channel as formation of a stripe quadrupole order: a wave of quadrupole moment without charge or spin modulation.

The iron-based superconductors (FeSCs) exhibit a complex phase diagram with multiple competing orders. For most of the FeSCs, an electronic nematic phase transition takes place at  $T_S$ , which is closely followed by a magnetic phase transition at  $T_N$  [1–4]. Superconductivity emerges in close proximity to the electronic nematic and the antiferromagnetic order. The highest superconducting (SC) transition temperature  $T_C$  often occurs when the nematic and the magnetic orders are fully suppressed but the orbital/charge or spin fluctuations remain strong [5–8]. The relationship between these fluctuations and superconductivity has been a focus of intense research [4, 9–14].

FeSe crystals provide the simplest case to elucidate the relationship between the orbital/charge order and superconductivity because it shows nematicity in the absence of magnetic order [9, 15, 16]. At ambient pressure, a structural phase transition that breaks the four-fold ( $C_4$ ) rotational symmetry takes place at  $T_S = 90$  K. Strong electronic quadrupole fluctuations involving the charge transfer between the Fe  $3d_{xz}$  and  $3d_{yz}$  orbitals, which contribute to most of the electronic density of states near  $E_F$ , have been observed above  $T_S$  [17–20]. The degeneracy of the  $d_{xz}$  and  $d_{yz}$  orbitals is lifted in the broken symmetry phase [21–24]. In the orthorhombic phase, although the lattice is only weakly distorted, prominent anisotropy is found for many electronic properties [23–27]. For crystals, superconductivity emerges in the nematic phase at  $T_C \approx 9$  K [15], while for FeSe monolayer films deposited on  $\text{SrTiO}_3$  substrate,  $T_C$  can be enhanced above 100 K [28–30]. Orbital selective SC pairing concentration has been reported by ARPES and quasiparticle interference (QPI) in bulk FeSe: the SC gap energy is large only for specific region of the nematic Fermi surfaces with the  $d_{yz}$  orbital characters [25, 27]. However, the mechanism behind the puzzling orbital selective superconductivity has not been discussed in depth.

In this Letter, we employ polarization-resolved Raman

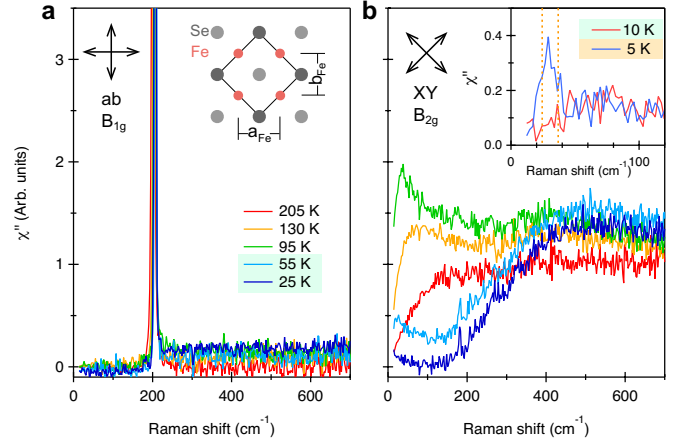


FIG. 1. Temperature evolution of the  $B_{1g}(ab)$  and  $B_{2g}(XY)$  symmetry Raman response  $\chi''(\omega, T)$  for pristine FeSe. Inset of Fig. 1a shows the top view of the FeSe layer. Dark and light gray circles represent the Se above and below the Fe layer. The 2-Fe unit cell is shown by solid lines. In the low temperature phase, the nearest Fe-Fe bond distance  $a_{Fe}$  becomes larger than  $b_{Fe}$  while  $a_{Fe}$  and  $b_{Fe}$  remain orthogonal. Inset of Fig 1b:  $\chi''(\omega, T)$  in the  $XY$  symmetry channel of FeSe in the normal state (10 K) and SC state (5 K). The magnitude of the two superconducting gaps  $2\Delta_{SC} = 3$  and 4.6 meV measured by tunneling spectroscopy are shown with the vertical dotted lines [27, 31].

spectroscopy to study charge quadrupole dynamics in non-magnetic superconductor  $\text{FeSe}_{1-x}\text{S}_x$  [17, 32]. We observe two main features in the  $XY$  symmetry scattering channel: a low-energy quasi-elastic peak (QEP) and a high-energy electronic continuum. Above  $T_S(x)$ , the QEP exhibits critical enhancement and softening upon cooling in wide temperature and doping range. Below  $T_S(x)$ , an unexpected gap gradually evolves in the spectra of the flat electronic continuum. Temperature dependence of the gap scales with the orthorhombic order parameter. The gap magnitude is proportional to  $T_S(x)$

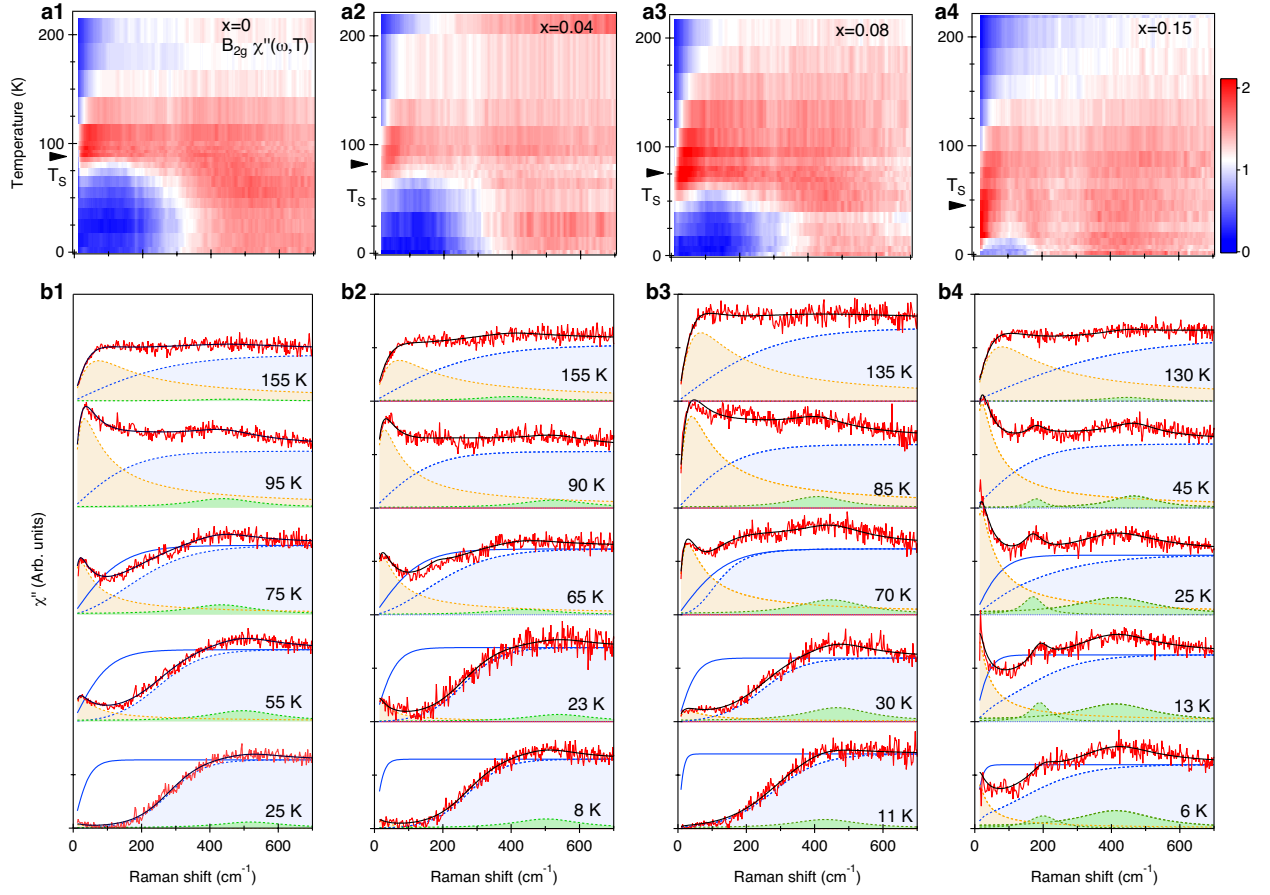


FIG. 2. (a1-a4) Temperature evolution of the XY symmetry Raman susceptibility  $\chi''(\omega, T)$  for FeSe $_{1-x}$ S $_x$  ( $x = 0, 0.04, 0.08$  and  $0.15$ ). Blue-white-red correspond to intensity from low to high. Arrows at the temperature axis denote  $T_S(x)$ . (b1-b4)  $\chi''(\omega, T)$  (red) at representative temperatures and their fits (black) with the decompositions of the QEP  $\chi''_{QEP}$  (orange shade) and the gapped continuum  $\Theta \chi''_C$  (blue shade). An oscillator  $\chi''_L$  (green shade) is included for the Lorentz peak near  $450 \text{ cm}^{-1}$  and the additional mode near  $190 \text{ cm}^{-1}$  for  $x = 0.15$ . For data at  $T < T_S$ , the blue solid curve shows the ungapped  $\chi''_C$ .

with the ratio  $2\Delta_x(0)/k_B T_S(x) = 4.8$ . We interpret the development of the gap in the quadrupole scattering channel as the formation of a stripe quadrupole (SQ) order below  $T_S(x)$ , which could provide explanations for the observed orbital selective superconductivity.

FeSe $_{1-x}$ S $_x$  ( $x = 0, 0.04, 0.08, 0.15$ ) single crystals were grown by chemical vapor transport technique as described in [17]. By substitution of sulfur for selenium,  $T_S$  is suppressed but the system remains non-magnetic, and superconductivity remains robust [17, 32]. The strain-free crystals were cleaved in nitrogen atmosphere and positioned in a continuous flow optical cryostat. Polarization-resolved Raman spectra were acquired in a quasi-backscattering geometry from the  $ab$  surface. We used 2.6 eV excitation from a Kr $^+$  laser. The laser power was kept below 10 mW for most measurements and less than 2 mW for the measurements in the superconducting state. The laser heating temperature  $\approx 1 \text{ K/mW}$  was calibrated by the appearance of the stripe pattern on the crystal surface at  $T_S$  [33]. The Raman scattering sig-

nal was analyzed by a custom triple-grating spectrometer and the data were corrected for the spectral response of the spectrometer.

Figs. 1a-b show the temperature dependence of the Raman response for the pristine FeSe in the  $B_{1g}$  ( $ab$ ) and  $B_{2g}$  ( $XY$ ) symmetry channels of the  $D_{4h}$  group.  $B_{1g}$  channel contains the Fe phonon ( $\approx 195 \text{ cm}^{-1}$ ) [35] on the background of a weak continuum (Fig. 1a). In contrast, the continuum in the  $B_{2g}$  channel (Fig. 1b) is strong and is composed of two main features with a remarkable temperature dependence:

- (1) *A low-energy quasi-elastic scattering peak (QEP).* The intensity of QEP is weak at high temperatures. Upon cooling, it softens, gains intensity, reaches its intensity maximum at just above  $T_S(x)$  and then gradually loses its intensity below  $T_S(x)$ . In the superconducting phase, the QEP acquires coherence and undergoes a metamorphosis into a coherent in-gap collective mode [36–40] (inset Fig. 1b).
- (2) *A nearly flat electronic continuum.* The intensity of

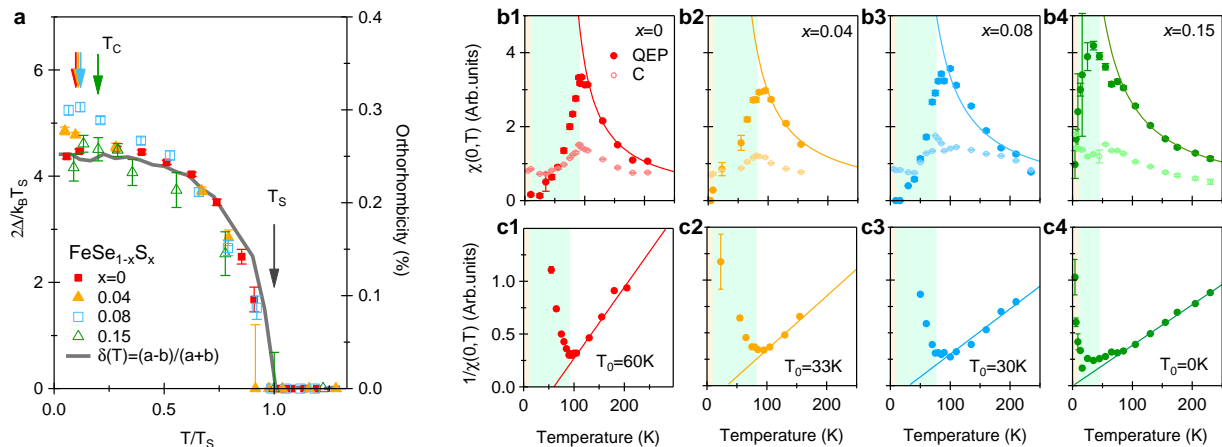


FIG. 3. (a) Temperature and doping evolution of the nematic gap  $2\Delta(T)/k_B T_S$  in  $\text{FeSe}_{1-x}\text{S}_x$  as a function of the reduced temperature  $T/T_S$ . The gray curve is the lattice order parameter  $\delta(T) = (a-b)/(a+b)$  for FeSe from ref [34].  $T_S$  and  $T_C$  are denoted by arrows. (b1-b4) The static Raman susceptibility  $\chi_{QEP}(0, T)$  and  $\chi_C(0, T)$  for  $x = 0, 0.04, 0.08$  and  $0.15$ . The Curie-Weiss fit for  $\chi_{QEP}(0, T)$  at  $T > T_S$  is shown by the solid curve. The yellow and cyan shades indicate  $T_C(x)$  and  $T_S(x)$ , respectively. (c1-c4) Temperature dependence of the inverse static susceptibility  $1/\chi_{QEP}(0, T)$  and the Weiss temperature  $T_0(x)$ . Error bars are the fitting standard error.

the continuum for 400-700  $\text{cm}^{-1}$  shows weak and monotonic increase with cooling above  $T_S(x)$ . Below  $T_S(x)$ , a significant gap suppression develops below 400  $\text{cm}^{-1}$ , and a broad peak centered near 450  $\text{cm}^{-1}$  appears.

For doped crystals, temperature evolution of the XY Raman response is quite similar to pristine FeSe (Figs. 2a1-a4). At the lowest temperature, a full gap suppression is observed for all doping concentrations except for  $x = 0.15$ , where a reduced scattering intensity remains in the gap, and an additional broad feature at around 190  $\text{cm}^{-1}$  appears below  $T_S$ .

We perform a multi-component fit to the XY symmetry Raman response (Figs. 2b1-b4). Here we represent QEP as a Drude function  $\chi_{QEP}''(\omega, T) = A_{QEP}^2 \omega \Gamma_{QEP} / (\omega^2 + \Gamma_{QEP}^2)$ , and the electronic continuum as a tanh function  $\chi_C''(\omega, T) = A_C^2 \tanh[\omega/\Gamma_C]$  plus a Lorentz oscillator  $\chi_L''(\omega, T)$  centered at 450  $\text{cm}^{-1}$ . Below  $T_S(x)$ , the gap-like suppression is modeled by  $\Theta(\omega, T) = \frac{1}{2}(1 + \tanh[\frac{\omega - 2\Delta(T)}{2k_B T_{eff}}])$  and applied to the continuum, where  $2\Delta(T)$  is the gap energy and  $T_{eff}$  is an effective temperature [31].

For all sulfur contents, the reduced gap energy  $2\Delta_x(T)/k_B T_S(x)$  collapses to a universal temperature dependence with  $2\Delta_x(0)/k_B T_S(x) = 4.8$  (Fig. 3a). The temperature dependence of  $2\Delta_x(T)$  follows the lattice order parameter  $\delta(T) = (a+b)/(a-b)$ [34], manifesting the direct connection between the formation of the gap and the lattice orthorhombicity.

We calculate the static Raman susceptibility for the QEP and the continuum contributions,  $\chi_{QEP}(0, T)$  and  $\chi_C(0, T)$ , by Kramers-Kronig transformation [31]. In contrast to the mild temperature evolution of  $\chi_C(0, T)$ , a

critical enhancement is seen above  $T_S(x)$  for  $\chi_{QEP}(0, T)$  (Figs. 3b1-b4). The temperature dependence of the QEP is generic for most FeSCs [5, 19, 33, 38, 41], and has been related to the ferro-quadrupole (FQ) fluctuations [12, 42–46]. The charge transfer between the nearly degenerated  $d_{xz}$  and  $d_{yz}$  orbitals creates a charge quadrupole with moment proportional to the local charge imbalance  $Q \propto n_{d_{xz}} - n_{d_{yz}}$ . In Fig. 4b we illustrate a snapshot of the FQ fluctuations. Such excitation results in a  $\Gamma_4^+(B_{2g})$  symmetry dynamic deformation of the Fermi surface pockets with nodal lines in the X/Y directions in the momentum space. We fit  $\chi_{QEP}(0, T > T_S)$  with a Curie-Weiss function  $\chi_{QEP}(0, T) = Q^2(x)/(T - T_0(x))$  (Fig. 3c1-c4), where  $T_0(x)$  is the Weiss temperature [5, 38].

In Fig. 4a we display the fitting parameters  $Q^2(x)$ ,  $2\Delta_x(0)$  and  $T_0(x)$  together with the  $\text{FeSe}_{1-x}\text{S}_x$  phase diagram.  $T_0(x)$  is tens of K below  $T_S$ , decreases with  $x$  and vanishes at  $x = 0.15$ , close to the nematic quantum critical point (QCP) as it was reported by elastoresistance study [17].  $Q^2(x)$  increases with  $x$  while  $2\Delta_x(0)$  decreases, implying the QEP and the gapped continuum arise from competing instabilities.

Now we turn to the origin of the gap. Appearance of the gap only in the XY symmetry channel reveals a density wave in either  $a$  or  $b$  direction [47]. Because neither charge nor spin modulation in the nematic phase was detected [15], we propose a collinear stripe  $d_{zx}/d_{yz}$  quadrupole order consisting of staggered  $Q$  and  $-Q$  quadrupole moments, as shown in Fig. 4c. The order parameter in real space can be defined as  $\phi_{XY} = \prod_{r=A \text{ site}} |Q_r\rangle \times \prod_{r=B \text{ site}} |\bar{Q}_r\rangle$ , which would give rise to the XY symmetry gap. Here  $Q/-Q$  quadrupole moments reside on iron sites  $r = A/B$ .

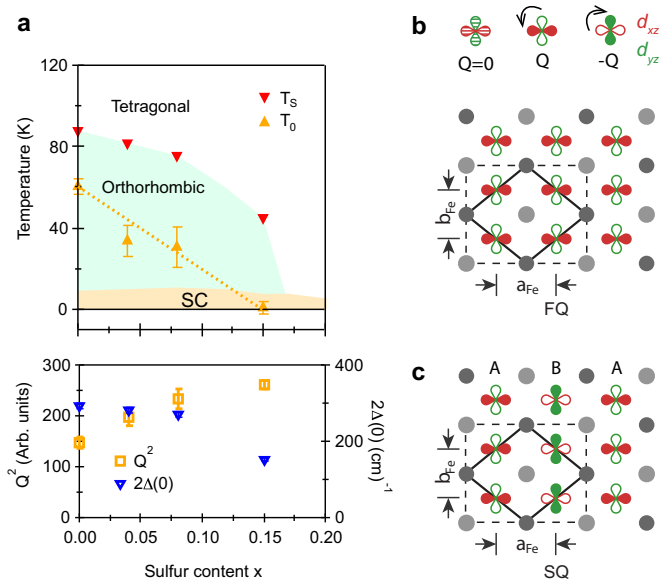


FIG. 4. (a) Phase diagram and the fitting parameters in  $\text{FeSe}_{1-x}\text{S}_x$ . The FQ moment  $Q^2(x)$  (empty squares, lower panel) and the Weiss temperature  $T_0(x)$  (upward triangles, upper panel) are obtained from the Curie-Weiss fit of  $\chi_{QEP}(0, T)$ .  $\Delta_x(0)$  (downward triangles, lower panel) is obtained from  $\Delta_x(T)$ . (b) A snapshot of the  $B_{2g}$  symmetry FQ fluctuations consist of  $d_{xz}/d_{yz}$  charge quadrupoles from the top view of a FeSe layer. An elementary quadrupole  $Q$  is created by in-site charge transfer from  $d_{yz}$  to  $d_{xz}$  orbital while a quadrupole  $-Q$  is created by charge transfer from  $d_{xz}$  to  $d_{yz}$  orbital. (c) SQ ground state with staggered  $|Q\rangle$  ( $A$  site) and  $|\bar{Q}\rangle$  ( $B$  site) in vertical stripes.  $a_{Fe} > b_{Fe}$ .

$XY$  symmetry Raman scattering directly couples to  $\Delta L = 2$  quadrupole excitations, making it a unique tool to probe the SQ order parameter or its dynamical fluctuations. In contrast, given that the total charge on each Fe site  $n_r = n_{r,d_{xz}} + n_{r,d_{yz}}$  is same, the charge sensitive probes such as scanning tunneling spectroscopy, X-ray diffraction or optical conductivity are unresponsive to such SQ order. We also notice that neutron scattering works suggest a hidden collinear antiferromagnetic quadrupole (AFQ) order for in FeSe [48, 49]. If the magnetic AFQ is at the same ordering vector as the charge SQ, a bilinear coupling between these two orders is allowed.

In the SQ-ordered phase, if the charge of the  $d_{xz}$  orbitals is modulated along the  $a$ -direction but remains invariant along the  $b$ -direction for the  $d_{yz}$  orbitals (Fig. 4c), the quasi-particle weight  $Z_{xz}$  resigning on the  $d_{xz}$  orbitals would be suppressed. The reduction of  $Z_{xz}$  would naturally result in a smaller SC gap for the  $d_{xz}$  orbitals [50] and overall in suppression of  $T_C$ , consistent with the observation of *orbital dependent superconducting gap* reported by ARPES and QPI [25, 27]. On the other hand, due to the coupling to the substrate, the SQ fluctuations are expected to be removed for the high  $T_C$  monolayer

FeSe films deposited on the  $\text{SrTiO}_3$ , resulting in a high- $T_C$  phenomenon [28, 29].

In summary, we use polarization-resolved Raman spectroscopy to study the evolution of charge dynamics in nonmagnetic  $\text{FeSe}_{1-x}\text{S}_x$  superconductor as a function of sulfur doping and temperature at above and below  $T_S(x)$ . We observe the development of a QEP on cooling towards  $T_S(x)$  and a pronounced gap in a flat continuum below  $T_S(x)$  in the  $XY$  symmetry Raman response. By increasing sulfur concentration, the QEP intensity is enhanced, but the gap magnitude and  $T_S(x)$  decrease. The appearance of robust low-energy gap implies the formation of a long-range quadrupole order, for example, a staggered stripe order. In the presence of the SQ order, the superconductivity on the  $d_{xz}$  orbital is suppressed due to the reduction of the quasiparticle weight along the SQ ordering vector direction, which provides a natural explanation for the observed orbital selective superconductivity in bulk FeSe [25, 27] as well as for the phenomena of high temperature superconductivity in monolayer FeSe films [28, 29] where the SQ order is expected to be suppressed due to the coupling to the substrate.

We thank A. V. Chubukov, M. Khodas, J. Schmalian, Q.-M. Si, T. P. Devereaux, K. Haule and H.-H. Kung for valuable discussions. The work at Rutgers was supported by the U.S. Department of Energy, Office of Basic Energy Sciences, Division of Materials Sciences and Engineering under Contract No. DE-SC0005463. The work in Japan was supported by Grant-in-Aids for Scientific Research (Proposals No. 15H02106, 15H03688, and 25220710), and by Grant-in-Aids on Innovative Areas ‘‘Topological Materials Science’’ (No. 15H05852), from Japan Society for the Promotion of Science (JSPS).

\* [wz131@physics.rutgers.edu](mailto:wz131@physics.rutgers.edu)

† On leave from Beijing National Laboratory for Condensed Matter Physics and Institute of Physics, Chinese Academy of Sciences, Beijing, 100190, China

‡ [girsh@physics.rutgers.edu](mailto:girsh@physics.rutgers.edu)

- [1] E. Fradkin, S. A. Kivelson, M. J. Lawler, J. P. Eisenstein, and A. P. Mackenzie, *Annu. Rev. Condens. Matter Phys.* **1**, 153 (2010).
- [2] G. R. Stewart, *Rev. Mod. Phys.* **83**, 1589 (2011).
- [3] J. Paglione and R. L. Greene, *Nat Phys* **6**, 645 (2010).
- [4] R. M. Fernandes, A. V. Chubukov, and J. Schmalian, *Nat. Phys.* **10**, 97 (2014).
- [5] Y. Gallais, R. M. Fernandes, I. Paul, L. Chauvière, Y.-X. Yang, M.-A. Méasson, M. Cazayous, A. Sacuto, D. Colson, and A. Forget, *Phys. Rev. Lett.* **111**, 267001 (2013).
- [6] A. E. Bohmer, P. Burger, F. Hardy, T. Wolf, P. Schweiss, R. Fromknecht, M. Reinecker, W. Schranz, and C. Meingast, *Phys. Rev. Lett.* **112**, 047001 (2014).
- [7] J.-H. Chu, H.-H. Kuo, J. G. Analytis, and I. R. Fisher, *Science* **337**, 710 (2012).
- [8] X. Lu, J. T. Park, R. Zhang, H. Luo, A. H. Nevidomskyy,

- Q. Si, and P. Dai, *Science* **345**, 657 (2014).
- [9] S.-H. Baek, D. V. Efremov, J. M. Ok, J. S. Kim, J. van den Brink, and B. Büchner, *Nat Mater* (2014).
- [10] A. E. Böhmer and C. Meingast, *Comptes Rendus Physique*, (2015).
- [11] A. V. Chubukov, M. Khodas, and R. M. Fernandes, *Phys. Rev. X* **6**, 041045 (2016).
- [12] Y. Gallais and I. Paul, *Comptes Rendus Physique* **17**, 113 (2016).
- [13] A. P. Dioguardi, T. Kissikov, C. H. Lin, K. R. Shirer, M. M. Lawson, H.-J. Grafe, J.-H. Chu, I. R. Fisher, R. M. Fernandes, and N. J. Curro, *Phys. Rev. Lett.* **116**, 107202 (2016).
- [14] L. Classen, R.-Q. Xing, M. Khodas, and A. V. Chubukov, *Phys. Rev. Lett.* **118**, 037001 (2017), and refs therein.
- [15] T. M. McQueen, A. J. Williams, P. W. Stephens, J. Tao, Y. Zhu, V. Ksenofontov, F. Casper, C. Felser, and R. J. Cava, *Phys. Rev. Lett.* **103**, 057002 (2009).
- [16] A. E. Böhmer, T. Arai, F. Hardy, T. Hattori, T. Iye, T. Wolf, H. v. Löhneysen, K. Ishida, and C. Meingast, *Phys. Rev. Lett.* **114**, 027001 (2015).
- [17] S. Hosoi, K. Matsuura, K. Ishida, H. Wang, Y. Mizukami, T. Watashige, S. Kasahara, Y. Matsuda, and T. Shibauchi, *Proc. Natl. Acad. Sci. USA* **113**, 8139 (2016).
- [18] M. A. Tanatar, A. E. Böhmer, E. I. Timmons, M. Schütt, G. Drachuck, V. Taufour, K. Kothapalli, A. Kreyssig, S. L. Bud'ko, P. C. Canfield, R. M. Fernandes, and R. Prozorov, *Phys. Rev. Lett.* **117**, 127001 (2016).
- [19] P. Massat, D. Farina, I. Paul, S. Karlsson, P. Strobel, P. Toulemonde, M.-A. Masson, M. Cazayous, A. Sacuto, S. Kasahara, T. Shibauchi, Y. Matsuda, and Y. Gallais, *Proc. Natl. Acad. Sci. USA* **113**, 9177 (2016).
- [20] A. Baum, H. N. Ruiz, N. Lazarević, Y. Wang, T. Böhm, R. Hosseinian Ahangharnejhad, P. Adelman, T. Wolf, Z. V. Popović, B. Moritz, T. P. Devereaux, and R. Hackl, *ArXiv e-prints* (2017), 1709.08998.
- [21] K. Nakayama, Y. Miyata, G. N. Phan, T. Sato, Y. Tanabe, T. Urata, K. Tanigaki, and T. Takahashi, *Phys. Rev. Lett.* **113**, 237001 (2014).
- [22] T. Shimojima, Y. Suzuki, T. Sonobe, A. Nakamura, M. Sakano, J. Omachi, K. Yoshioka, M. Kuwata-Gonokami, K. Ono, H. Kumigashira, A. E. Böhmer, F. Hardy, T. Wolf, C. Meingast, H. v. Löhneysen, H. Ikeda, and K. Ishizaka, *Phys. Rev. B* **90**, 121111 (2014).
- [23] M. D. Watson, T. K. Kim, A. A. Haghighirad, N. R. Davies, A. McCollam, A. Narayanan, S. F. Blake, Y. L. Chen, S. Ghannadzadeh, A. J. Schofield, M. Hoesch, C. Meingast, T. Wolf, and A. I. Coldea, *Phys. Rev. B* **91**, 155106 (2015).
- [24] Y. Suzuki, T. Shimojima, T. Sonobe, A. Nakamura, M. Sakano, H. Tsuji, J. Omachi, K. Yoshioka, M. Kuwata-Gonokami, T. Watashige, R. Kobayashi, S. Kasahara, T. Shibauchi, Y. Matsuda, Y. Yamakawa, H. Kontani, and K. Ishizaka, *Phys. Rev. B* **92**, 205117 (2015).
- [25] H. C. Xu, X. H. Niu, D. F. Xu, J. Jiang, Q. Yao, Q. Y. Chen, Q. Song, M. Abdel-Hafiez, D. A. Chareev, A. N. Vasiliev, Q. S. Wang, H. L. Wo, J. Zhao, R. Peng, and D. L. Feng, *Phys. Rev. Lett.* **117**, 157003 (2016).
- [26] A. Fedorov, A. Yaresko, T. K. Kim, Y. Kushnirenko, E. Haubold, T. Wolf, M. Hoesch, A. Grüneis, B. Büchner, and S. V. Borisenko, *Sci. Rep.* **6**, 36834 (2016).
- [27] P. O. Sprau, A. Kostin, A. Kreisel, A. E. Böhmer, V. Taufour, P. C. Canfield, S. Mukherjee, P. J. Hirschfeld, B. M. Andersen, and J. C. S. Davis, *Science* **357**, 75 (2017).
- [28] W. Qing-Yan, L. Zhi, Z. Wen-Hao, Z. Zuo-Cheng, Z. Jin-Song, L. Wei, D. Hao, O. Yun-Bo, D. Peng, C. Kai, W. Jing, S. Can-Li, H. Ke, J. Jin-Feng, J. Shuai-Hua, W. Ya-Yu, W. Li-Li, C. Xi, M. Xu-Cun, and X. Qi-Kun, *Chin. Phys. Lett.* **29**, 037402 (2012).
- [29] J.-F. Ge, Z.-L. Liu, C. Liu, C.-L. Gao, D. Qian, Q.-K. Xue, Y. Liu, and J.-F. Jia, *Nat Mater* **14**, 285 (2015).
- [30] D.-H. Lee, *Science* **357**, 32 (2017).
- [31] See Supplemental Material at [url put by publisher] for details of data analysis, phonon spectra and the spectra in the superconducting state.
- [32] K. Matsuura, Y. Mizukami, Y. Arai, Y. Sugimura, N. Maejima, A. Machida, T. Watanuki, T. Fukuda, T. Yajima, Z. Hiroi, K. Y. Yip, Y. C. Chan, Q. Niu, S. Hosoi, K. Ishida, K. Mukasa, T. Watashige, S. Kasahara, J.-G. Cheng, S. K. Goh, Y. Matsuda, Y. Uwatoko, and T. Shibauchi, *ArXiv e-prints* (2017), 1704.02057.
- [33] F. Kretzschmar, T. Böhm, U. Karahasanovic, B. Muschler, A. Baum, D. Jost, J. Schmalian, S. Caprara, M. Grilli, C. Di Castro, J. G. Analytis, J. H. Chu, I. R. Fisher, and R. Hackl, *Nat. Phys.* **12**, 560 (2016).
- [34] Q. Wang, Y. Shen, B. Pan, Y. Hao, M. Ma, F. Zhou, P. Steffens, K. Schmalzl, T. R. Forrest, M. Abdel-Hafiez, X. Chen, D. A. Chareev, A. N. Vasiliev, P. Bourges, Y. Sidis, H. Cao, and J. Zhao, *Nat. Mater* **15**, 159 (2016).
- [35] V. Gnezdilov, Y. G. Pashkevich, P. Lemmens, D. Wulferding, T. Shevtsova, A. Gusev, D. Chareev, and A. Vasiliev, *Phys. Rev. B* **87**, 144508 (2013).
- [36] F. Kretzschmar, B. Muschler, T. Böhm, A. Baum, R. Hackl, H.-H. Wen, V. Tsurkan, J. Deisenhofer, and A. Loidl, *Phys. Rev. Lett.* **110**, 187002 (2013).
- [37] A. Hinojosa, J. Cai, and A. V. Chubukov, *Phys. Rev. B* **93**, 075106 (2016).
- [38] V. K. Thorsmølle, M. Khodas, Z. P. Yin, C. Zhang, S. V. Carr, P. Dai, and G. Blumberg, *Phys. Rev. B* **93**, 054515 (2016).
- [39] Y. Gallais, I. Paul, L. Chauvière, and J. Schmalian, *Phys. Rev. Lett.* **116**, 017001 (2016).
- [40] S.-F. Wu, P. Richard, H. Ding, H.-H. Wen, G. Tan, M. Wang, C. Zhang, P. Dai, and G. Blumberg, *Phys. Rev. B* **95**, 085125 (2017).
- [41] W.-L. Zhang, P. Richard, H. Ding, A. S. Sefat, J. Gillett, S. E. Sebastian, M. Khodas, and G. Blumberg, *ArXiv e-prints* (2014), arXiv:1410.6452.
- [42] C.-C. Lee, W.-G. Yin, and W. Ku, *Phys. Rev. Lett.* **103**, 267001 (2009).
- [43] W. Lv, J. Wu, and P. Phillips, *Phys. Rev. B* **80**, 224506 (2009).
- [44] T. Saito, S. Onari, and H. Kontani, *Phys. Rev. B* **82**, 144510 (2010).
- [45] H. Kontani and Y. Yamakawa, *Phys. Rev. Lett.* **113**, 047001 (2014).
- [46] H. Yamase and R. Zeyher, *Phys. Rev. B* **88**, 125120 (2013).
- [47] W.-L. Zhang, Z. P. Yin, A. Ignatov, Z. Bukowski, J. Karpinski, A. S. Sefat, H. Ding, P. Richard, and G. Blumberg, *Phys. Rev. B* **93**, 205106 (2016).
- [48] R. Yu and Q. Si, *Phys. Rev. Lett.* **115**, 116401 (2015).
- [49] Q. Wang, Y. Shen, B. Pan, X. Zhang, K. Ikeuchi,

- K. Iida, A. D. Christianson, H. C. Walker, D. T. Adroja, M. Abdel-Hafez, X. Chen, D. A. Chareev, A. N. Vasiliev, and J. Zhao, [Nat. Commun. \*\*7\*\*, 12182 \(2016\)](#).
- [50] A. Kreisel, B. M. Andersen, P. O. Sprau, A. Kostin, J. C. S. Davis, and P. J. Hirschfeld, [Phys. Rev. B \*\*95\*\*, 174504 \(2017\)](#).

## SUPPLEMENTAL MATERIALS

### I. Background subtraction

The imaginary part of the Raman susceptibility  $\chi''_{\mu\nu}(\omega, T)$  can be calculated from the total secondary emission intensity  $I_{\mu\nu}(\omega, T) = [1 + n(\omega, T)]\chi''_{\mu\nu}(\omega, T) + I_{lumi}$ , where  $\mu(\nu)$  denotes the polarization of the incident and scattered light,  $[1 + n(\omega, T)] = [1 - \exp(-h\omega/k_B T)]^{-1}$  is the Bose distribution function for Stokes Raman scattering and  $I_{lumi}$  is the luminescence background. The scattering intensity has been corrected for the system response and normalized by the incident laser power and the acquisition time.

Raman scattering spectra were acquired in three polarization configurations:  $\mu\nu = XY, ab$  and  $aa$ , to separate excitations in distinct symmetry channels:  $B_{1g} = ab$ ,  $B_{2g} = XY$ , and  $A_{1g} = aa(bb) - XY$ . In Fig. S1a and b we show the secondary emission intensity for the  $ab$  and  $XY$  geometries at various temperatures for the pristine FeSe.

The  $ab$  geometry scattering continuum is almost independent of temperature, therefore we attribute it to the luminescence. Assuming that the luminescence is same for  $XY$  and  $ab$  geometries, we calculate the Raman re-

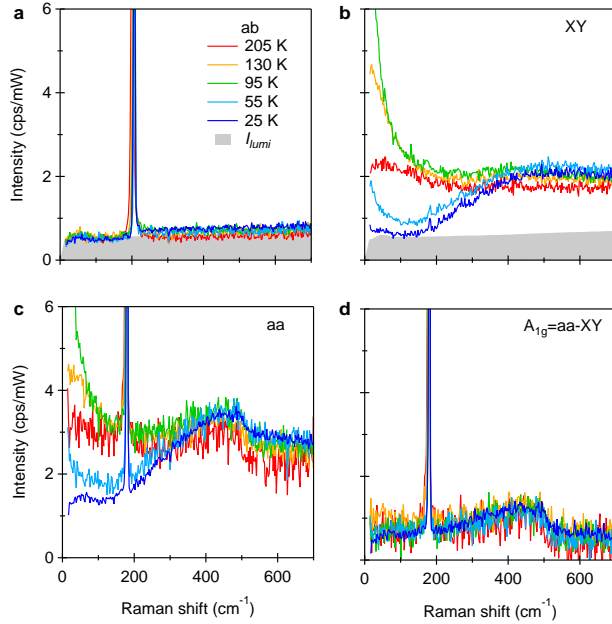


FIG. S1. (a-c) The secondary emission intensity for the  $ab$ ,  $XY$  and  $aa$  scattering geometries in pristine FeSe. The luminescence background calculated for  $ab$  and  $XY$  scattering geometries is calculated from the scattering continuum in the  $ab$  geometry. (d)  $A_{1g}$  symmetry scattering intensity calculated from the secondary emission intensity in  $aa$  and  $XY$  geometries.

sponse in the  $ab$  and  $XY$  scattering geometries with a temperature independent luminescence background estimated by the lowest  $ab$  geometry scattering continuum ( $B_{1g}$  phonon subtracted), as shown by the grey shade in Figs. S1a and b.

The  $A_{1g}$  symmetry scattering intensity is calculated by subtracting the  $XY$  symmetry secondary emission intensity from  $aa$ , as shown in Figs. S1c and d.

### II. Doping dependence of phonon spectra

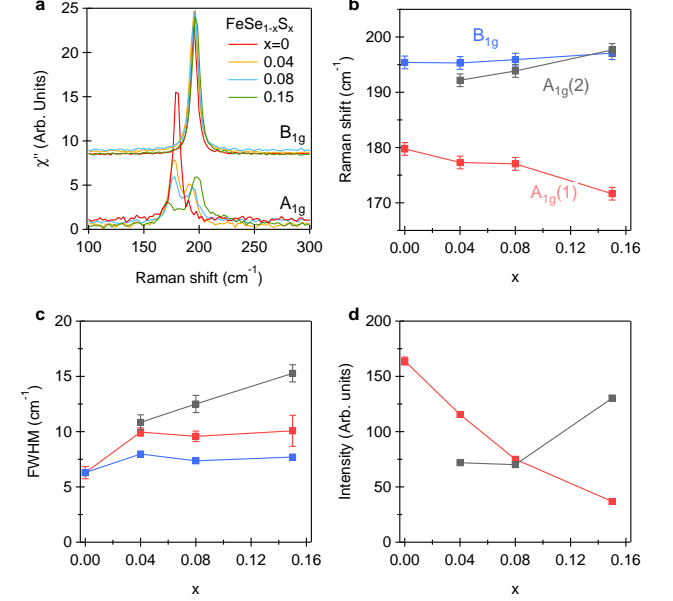


FIG. S2. (a)  $A_{1g}$  and  $B_{1g}$  symmetry phonon spectra at room temperature. The  $B_{1g}$  spectra are offset in the vertical direction. (b-c) Doping dependence of the energy and line width of the  $B_{1g}$  and two  $A_{1g}$  phonons. (c) The integrated intensity of the two  $A_{1g}$  phonons. Error bars in (b) are determined by the instrument energy resolution  $2.3 \text{ cm}^{-1}$ . Error bars in (c) and (d) are the fitting standard errors.

We observe two Raman active phonons from  $ab$  plane at room temperature in the pristine FeSe: one  $A_{1g}$  phonon at around  $180 \text{ cm}^{-1}$  of Se vibration and one  $B_{1g}$  phonon at around  $195 \text{ cm}^{-1}$  of Fe vibration [35]. With sulfur substitution, the energy of the  $B_{1g}$  phonon only changes slightly, while the  $A_{1g}$  phonon gradually softens and loses intensity. A new  $A_{1g}$  phonon mode appears at around  $193 \text{ cm}^{-1}$ , its intensity increases with  $x$  (Fig. S2).

### III. Data fit

Above  $T_S$ ,  $\chi''(\omega, T)$  is fitted with

$$\chi''(\omega, T > T_S) = \chi''_{QEP}(\omega, T) + \chi''_C(\omega, T) + \chi''_L(\omega, T), \quad (1)$$

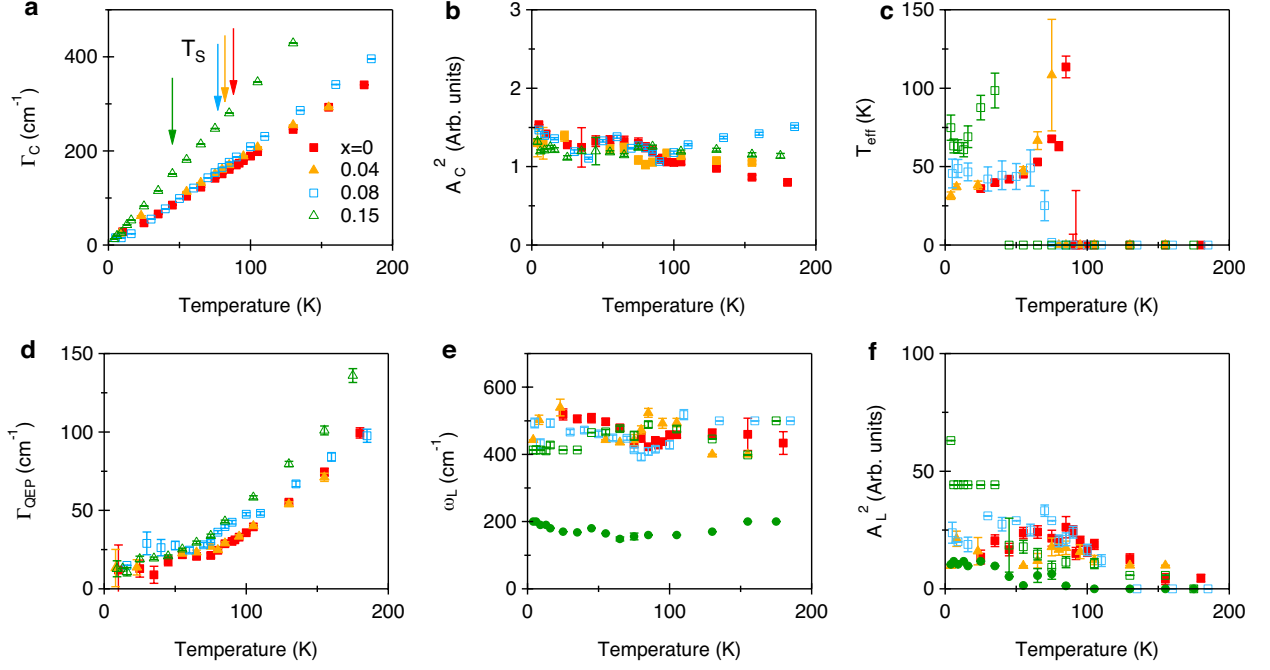


FIG. S3. Fitting parameters as a function of temperature and sulfur content. Error bars are the fitting standard errors.

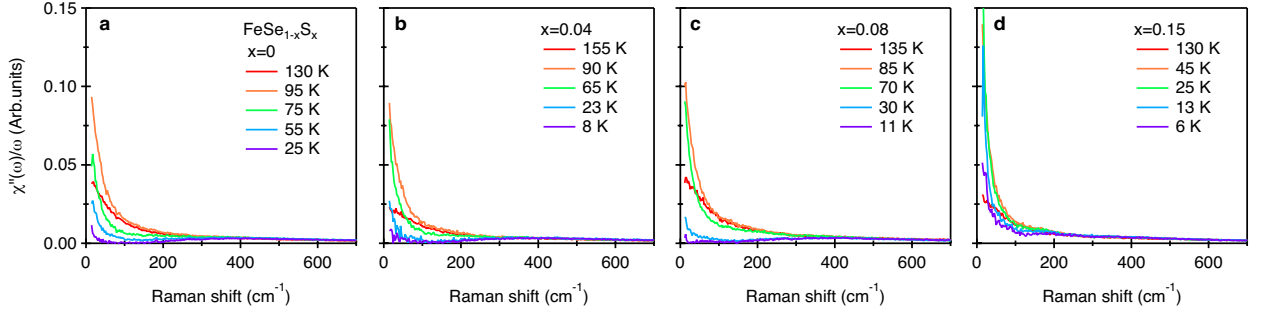


FIG. S4.  $\chi''(\omega, T)$  at selected temperatures for  $x = 0, 0.04, 0.08$  and  $0.15$ .

Below  $T_S$ ,  $\chi''(\omega, T)$  is fitted with

$$\chi''(\omega, T < T_S) = \chi''_{QEP}(\omega, T) + \chi''_C(\omega, T)\Theta(\omega, T) + \chi''_L(\omega, T) \quad (2)$$

Here

$$\chi''_{QEP}(\omega, T) = A_{QEP}^2(T) \frac{\omega \Gamma_{QEP}(T)}{\omega^2 + \Gamma_{QEP}^2(T)}, \quad (3)$$

$$\chi''_C(\omega, T) = A_C^2(T) \tanh[\omega/\Gamma_C(T)], \quad (4)$$

$$\chi''_L(\omega, T) = A_L^2 \left[ \frac{1}{[\omega - \omega_L(T)]^2 + \Gamma_L^2(T)} - \frac{1}{[\omega + \omega_L(T)]^2 + \Gamma_L^2(T)} \right], \quad (5)$$

and

$$\Theta(\omega, T) = \frac{1}{2} \left( 1 + \tanh \left[ \frac{\omega - 2\Delta(T)}{2k_B T_{eff}} \right] \right). \quad (6)$$

For  $T > T_S$ , all fitting parameters are set to be free.  $\Gamma_C(T)$  shows a linear temperature dependence  $\Gamma_C(T > T_S) = k_C T$ . For  $T < T_S$ , we constrain  $\Gamma_C(T)$  from linear extrapolated of  $\Gamma_C(T > T_S)$  and the other fitting parameters are set to be free.

In Fig. S3 we show the fitting parameters. The effective temperature for the nematic gap decreases with lowering the temperature and is much larger than the real temperature (Fig. S3c).  $A_C$  is almost invariant of temperature and sulfur substitution (Fig. S3b). For above  $T_S$ ,  $\Gamma_{QEP}$  is linear of temperature. On entering into the nematic state, the linear decreasing of  $\Gamma_{QEP}$  slows down. At slightly above  $T_C$ ,  $\Gamma_{QEP}$  converges to a consistent value  $12 \text{ cm}^{-1}$  (Fig. S3d). In Fig. S3e and f we show the temperature dependence of the central frequency  $\omega_L(T)$  and intensity  $A_L^2(T)$ .

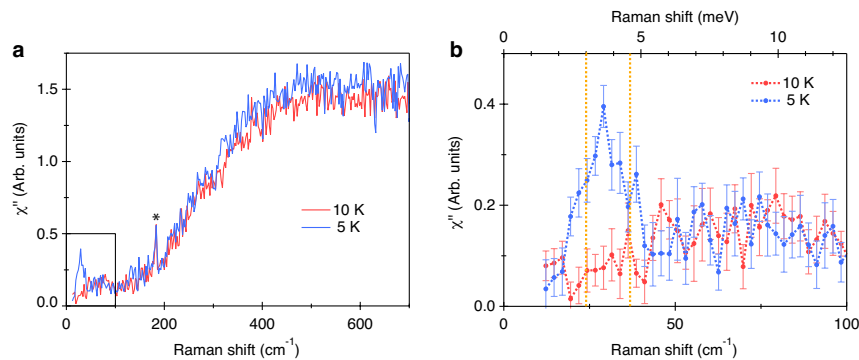


FIG. S5. (a)  $XY$  symmetry Raman response in FeSe at 10 K (normal state) and 5 K (superconducting state). (b) Zoom in of the spectra in (a). The error bars are calculated from the standard deviation. The magnitudes of the superconducting gaps  $2\Delta_{SC} = 3$  and  $4.6$  meV defined by the scanning tunneling spectroscopy [27] are shown by the vertical dotted lines.

#### IV. Static susceptibility

Raman scattering measures the imaginary part of the susceptibility  $\chi''(\omega)$ . The real part of the susceptibility  $\chi'(\omega)$  is connected to the  $\chi''(\omega)$  by Kramers-Kronig transformation. We calculate the static susceptibility  $\chi(0)$  by

$$\chi(0) = \frac{2}{\pi} P \int_0^{\omega_1} \frac{\chi''(\omega)}{\omega} d\omega, \quad (7)$$

where  $\omega_1$  is a high-energy cut-off. For the QEP that has a Drude form (Eq. 4),  $\chi_{QEP}(0) = A_{QEP}^2$  is derived from the analytical function. We perform a numerical integration to calculate  $\chi_C(0, T)$ . As shown in Fig. S4,  $\chi''(\omega)/\omega$  for above  $600 \text{ cm}^{-1}$  is small and independent of temperature, therefore we choose a high-energy cut-off  $\omega_1 = 600 \text{ cm}^{-1}$ . For the response function below the low-energy measurement limit, we use a linear extrapolation

determined from the fitting parameter of  $\chi_C''(\omega, T)$ .

#### V. Response in the superconducting phase

Fig. S5 displays the  $XY$  symmetry Raman response at 10 K (normal state) and 5 K (superconducting state). In the superconducting state, the QEP is completely removed and a sharp symmetric peak at  $29 \text{ cm}^{-1}$  (3.6 meV) appears. The mode energy is between the two superconducting gap values  $2\Delta_{SC} = 3$  and  $4.6$  meV determined by tunneling spectroscopy [27]. Therefore, it is attributed to the nematic resonance mode that appears in the superconducting state when the critical damping is removed [36–40]. The mode at  $183.5 \text{ cm}^{-1}$  marked with an asterisk in Fig. S5a is the  $A_g$  symmetry phonon mode due to the merging of the  $A_{1g}$  and  $B_{2g}$  symmetry channels when the high-temperature  $D_{4h}$  group is reduced to the low-temperature  $D_{2h}$  group.